# Nano-Micro Letters

ARTICLE

Liquid Metal Grid Patterned Thin Film Devices Toward Absorption-Dominant and Strain-Tunable Electromagnetic Interference Shielding

Yuwen Wei[1], Priyanuj Bhuyan[2], Suk Jin Kwon[3], Sihyun Kim[1], Yejin Bae[1], Mukesh Singh[2], Duy Thanh Tran[1], Minjeong Ha[4], Kwang-Un Jeong[1], Xing Ma[5], Byeongjin Park[3] ✉, Sungjune Park[2] ✉

HIGHLIGHTS

- Multiple internal reflection-based absorption-dominant stretchable electromagnetic shielding thin film by incorporating liquid metal grid structure is developed.

- The device demonstrates high electromagnetic shielding effectiveness (SE) (SE_T of up to 75 dB) with low reflectance (SE_R of 1.5 dB at the resonant frequency).

- The shielding properties of the device can be tuned by adjusting the liquid metal patterned grid spaces upon strain.

ABSTRACT The demand of high-performance thin-film-shaped deformable electromagnetic interference (EMI) shielding devices is increasing for the next generation of wearable and miniaturized soft electronics. Although highly reflective conductive materials can effectively shield EMI, they prevent deformation of the devices owing to rigidity and generate secondary electromagnetic pollution simultaneously. Herein, soft and stretchable EMI shielding thin film devices with absorption-dominant EMI shielding behavior is presented. The devices consist of liquid metal (LM) layer and LM grid-patterned layer separated by a thin elastomeric film, fabricated by leveraging superior adhesion of aerosol-deposited LM on elastomer. The

devices demonstrate high electromagnetic shielding effectiveness (SE) (SE_T of up to 75 dB) with low reflectance (SE_R of 1.5 dB at the resonant frequency) owing to EMI absorption induced by multiple internal reflection generated in the LM grid architectures. Remarkably, the excellent stretchability of the LM-based devices facilitates tunable EMI shielding abilities through grid space adjustment upon strain (resonant frequency shift from 81.3 to 71.3 GHz @ 33% strain) and is also capable of retaining shielding effectiveness even after multiple strain cycles. This newly explored device presents an advanced paradigm for powerful EMI shielding performance for next-generation smart electronics.
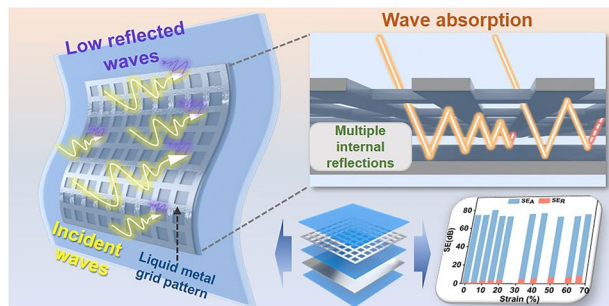
KEYWORDS Absorption-dominant electromagnetic interference shielding; Liquid metals; Soft and stretchable electronics; Thin film devices; Tunable electromagnetic interference shielding

Yuwen Wei and Priyanuj Bhuyan contributed to this equally.

✉ Byeongjin Park, b.park@kims.re.kr; Sungjune Park, sungjunepark@skku.edu

1 Department of Polymer-Nano Science and Technology, Department of Nano Convergence Engineering, Jeonbuk National University, Jeonju 54896, Republic of Korea

2 School of Chemical Engineering, Sungkyunkwan University (SKKU), Suwon 16419, Republic of Korea

3 Composites Research Division, Korea Institute of Materials Science, Changwon 51508, Republic of Korea

4 School of Materials Science and Engineering, Gwangju Institute of Science and Technology, Gwangju 61005, Republic of Korea

5 School of Materials Science and Engineering, and Sauvage Laboratory for Smart Materials, Harbin Institute of Technology (Shenzhen), Shenzhen, Guangdong 518055, People's Republic of China

1 Introduction

Recently, intelligent electronic devices have been growing rapidly to meet the demand in various fields ranging from communication facilities and wireless networks to portable and wearable hardware. However, the adverse effect encountered as a result of escalated use of these devices is the rise in electromagnetic pollution arising from electromagnetic interference (EMI), which not only threatens the functionality and durability of electronic devices, but also affects several biological processes in living beings [1–3]. As a result, development of EMI shielding materials has received a tremendous boost [4–10]. Specially, EMI shields fabricated out of thin film materials are the current research hotspots that aim to match the trend of uprising conformal and highly integrated compact electronics, ranging from wearable devices to high-end military and aerospace applications [11, 12]. At the same time, the need for real-time adjustable shielding performance to address intelligent application requirements like passing serviceable EM waves [13], information leakage suppression [14, 15], etc., has led to growing demand of engineering of EMI shielding materials with adjustable shielding properties. Therefore, development of soft, stretchable, and thin film-shaped EMI shielding materials with the ability to modulate shielding abilities can cater the demand of next-generation electronic systems.

While conventional metals and their alloys can function effectively as shielding materials due to their superior electrical conductivity, inadequate resistance to corrosion and limited deformability constrain their applicability in EMI shielding [16, 17]. Additionally, high reflectivity of metals leads to secondary electromagnetic pollution [17]. In lieu of the use of metals, polymer-based EMI shielding materials, with various conductive fillers such as graphene, carbon fibers, carbon nanotubes, and MXenes arranged into segregated structures or preferred orientations within the polymeric matrices, are widely used owing to their distinctive attributes like exceptional corrosion resistance, adequate deformability for application in conformal and wearable electronics, and tunable EMI shielding performances such as modulating the shielding effectiveness, and resonant frequency. [11, 18–24]. Additionally, the filler properties like surface morphology, aggregation, alignments, etc., can be specifically tuned to target electromagnetic waves in different bands or frequency ranges [25–28]. Recently, efforts have been made to develop

such polymer-particle-based hybrid EMI shielding materials with low reflectivity through multiple internal reflections [29, 30], but in most cases, low reflectivity is simultaneously associated with low absorptivity of the conducting materials [31, 32]. While MXenes, a class of two-dimensional conductive materials, exhibit enhanced absorption efficiency, their oxidation-induced degradation under environmental conditions significantly limits their potential for practical applications [33, 34]. At the same time, incorporating these fillers to achieve higher shielding performances either requires higher filler to polymer ratio or micro-level engineering for specific filler orientations, which often makes fabrication and processing steps challenging. Moreover, their repeated deformations may degrade overall electro-mechanical properties of the composites due to various factors like misorientation of the trapped fillers, debonding at the polymer-filler interfaces, micro-crack initiation and propagation, etc., thereby threatening their longtime usage [21].

To address the aforementioned issues, it is not only necessary to explore conductive materials that can effectively shield under deformation, but also deduce methodologies that can utilize these materials to achieve low reflectivity-based EMI shielding functionality. For the first case, liquid metal (LM), a promising candidate due to its commendable electrical conductivity and fluidity [35–43], has recently emerged as the forefront material for development of soft and stretchable EMI shielding materials [44–48]. However, given its metallic properties, this class of materials still exhibit high reflectivity. As a solution to the second case, foam structures have been widely used as effective absorption-dominant materials, but their high void content increases their thickness [49, 50]. A few recent studies suggest an alternative approach of usage of conductive grid patterns to achieve low reflection and high absorption at specific frequencies where the minimum reflection is achieved at the resonant frequency on matching the wavelength of the electromagnetic wave (EMW) with the grid period [24, 29]. This method is quite promising in terms of significantly reducing the size of the device, however, certain challenges persist, viz., poor choice of materials that can challenge the structural stability for prolonged use and time-intensive, optimization-critical printing technologies.

This study presents a soft and stretchable thin-film-shaped liquid metal grid-patterned device (LMGD) for effective EMI shielding, featuring low reflectivity and superior

absorption-dominant shielding effects. The LMGD, comprising a liquid metal layer and grid pattern separated by an elastomer layer, achieved high electromagnetic shielding effectiveness (SE) up to 75 dB due to multiple internal reflection-induced absorption behavior. The LM grid structure is obtained via aerosol deposition of LM using an airbrush through recyclable OHP line-stencils, offering rapid and cost-effective fabrication compared to conventional printing methods. With minimal electromagnetic wave reflection ($SE_R < 1.5$ dB at resonant frequency) determined by the LM grid geometries, the LMGD's stretchable and highly elastic properties enabled tunable shielding abilities by adjusting grid spacing under strain. Notably, at a strain value of 10%, the resonant frequency recorded 77 GHz, which corresponds to automotive radar band used in self-driving cars with ADAS (Advanced Driver Assistance System) [51, 52]. Additionally, it exhibits excellent shielding retention after multiple strain cycles, attributed to the preserved continuity of embedded LM structures. To the best of our knowledge, this study reports a significant advancement in the field of EMI shielding devices, exhibiting the highest performances of SE in terms of low reflection, high absorption properties, and SE stability and retention maintained after repeated external deformations.

2 Experimental Section

2.1 Materials

Eutectic Gallium Indium alloy (EGaIn) was obtained from Indium Corporation, USA. DragonSkin 10 medium, an ultrastretchable two-component elastomer, was obtained from Hyup Shin, Korea. OHP sheets for preparing stencils were obtained from Coupang, Korea. All the samples were casted in laboratory-scale square-shaped petri dishes.

2.2 Fabrication of LMGD

Uncured silicone elastomer was first prepared by mixing components A and B in a 1:1 weight ratio in a paper cup. After thorough stirring, the resulting mixture was spin-coated onto an acrylic plate (10 cm × 10 cm, coated with Ease-Release, a general-purpose releasing agent) using a spin coater (Dongah Trade Corp ACE-200) at 1000 rpm

for 90 s. Subsequently, the spin-coated elastomer layer was cured in an oven at 100 °C for 5 min to render a thin, semicured silicone layer. The OHP film stencil (designed using Silhouette Cameo 4), consisting of parallel negative spaces, was positioned precisely on the elastomer film, and EGaIn was evenly distributed on the surface using an airbrush (Monster Brush 001) by maintaining a distance of 15 cm from the substrate. The stencil was then rotated by 90° and LM was re-spray-coated to obtain the grid design. Finally, uncured silicone was spin-coated after removing the stencil and subsequently cured to produce the LM grid elastomer film. To obtain the secondary LM layer, another stencil consisting of negative space equivalent to the desired area was used to spray coat LM on the first film and then encapsulated by elastomer, realizing the final device. The detailed process is illustrated in Fig. 1 along with its technical aspects and advantages in the introduction section. For EMI SE measurements, square samples having dimensions 10 cm × 10 cm were prepared, whereas for mechanical and electrical characterizations, smaller samples of 2.5 cm × 2.5 cm were prepared to fit the grippers of universal testing machine.

2.3 Characterization

The EMI SE measurements were carried out using Keysight N5291A vector network analyzer assisted by a free space measurement system (EMLabs FS-110). All resistance-related measurements were carried out using benchtop multimeter (Keysight 34461a). The mechanical properties of the samples were assessed using a universal testing machine (Quasar 2.5 single column). Tilting and adhesion test images were captured using a Phoenix 300 tilting contact angle measurement system, and all microscopic images were captured using an Olympus CX23 instrument.

2.4 Measurement of EMI SE

The network analyser method was used in this study for far-field EMI SE measurements. The EMI shielding effectiveness in the far field can be calculated by measuring the scattering parameters (S_{11}, S_{21}, S_{22}, S_{12}), based on which reflectance (R), transmittance (T), and absorbance (A) were calculated according to the following equations [53, 54]:
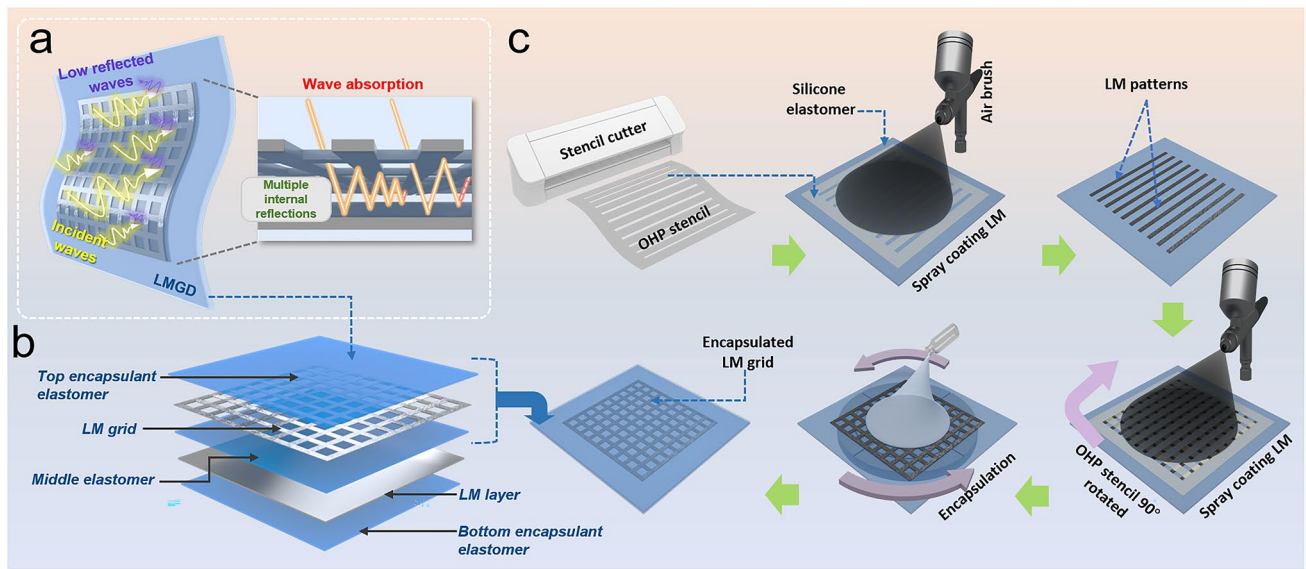
Fig. 1 **a** Schematic diagram illustrating the concept of maximization of incident EM wave absorption with lower reflected waves through multiple internal reflections in LMGD. **b** Schematic diagram showing the different components of the designed LMGD. **c** Schematic diagram illustrating the grid architecture fabrication using two-step spray coating of LM on a stretchable and elastic substrate through recyclable OHP stencil

$$R = |S_{11}|^2 = |S_{22}|^2 \tag{1}$$

$$T = |S_{12}|^2 = |S_{21}|^2 \tag{2}$$

$$A = 1 - R - T \tag{3}$$

Total shielding effectiveness SE_T, reflective shielding effectiveness SE_R, and absorptive shielding effectiveness SE_A can be calculated using T, R, and A, respectively, according to the following equations:

$$SE_T = 10\log\left(\frac{1}{T}\right) = 10\log\left(\frac{1}{|S_{12}|^2}\right) \tag{4}$$

$$SE_R = 10\log\left(\frac{1}{1-R}\right) = 10\log\left(\frac{1}{1-|S_{11}|^2}\right) \tag{5}$$

$$SE_A = 10\log\left(\frac{1-R}{T}\right) = 10\log\left(\frac{1-|S_{11}|^2}{|S_{12}|^2}\right) \tag{6}$$

$$SE_T = SE_R + SE_A \tag{7}$$

3 Results and Discussion

3.1 LMGD Designing

Figure 1a illustrates the proposed concept of using an LM grid and an LM layer to maximize the absorption of incident EM waves through multiple internal reflections within the device. As shown in Fig. 1b, the LM grid and the LM layer are separated by an elastomeric layer that acts as a physical separator between the LM grid and the LM layer and facilitates space for the multiple internal reflection to occur. The grid structure is capable of acting as an inductive filter circuit, allowing EM waves of specific wavelengths ideally matching with grid period to pass through it [29, 55], while encountering reflection in the LM layer behind to enable multiple internal reflections or scattering within the device between the grid and layer. Figure 1c describes the overall fabrication process of LMGD film-type EMI shielding device. In order to guarantee both safety and durability of the device for prolonged utility and the ability to adapt to stretching of various degrees, DragonSkin—an ultrastrechable silicone—was chosen as the matrix elastomer due to its exceptional stretchability and easy processing. In order to embed desired LM designs in the elastomer, there are

number of methods to choose from that have emerged in the recent years. Although replica molding followed by plasma bonding for fabricating soft microfluidic channels in rigid silicones, followed by injection of LM through them is a commonly employed technique to obtain stretchable and conductive LM patterns, the method encounters several challenges when applied to materials like soft and stretchable silicones (e.g., DragonSkin or Ecoflex) [56]. Silicone oils present in such soft silicones can migrate to the surface during plasma treatment, causing interference with the plasma bonding process [57]. Moreover, injecting LM poses a risk of damaging the device due to the injection hole, potentially compromising its mechanical properties. At the same time, high pressures required to fully inject LM cannot be sustained by the thinness and the intrinsic low elastic modulus of the elastomers. Therefore, a modified lithography-free method to fabricate liquid metal designs on the silicone elastomer was adopted that followed a two-step spray coating of LM through a recyclable OHP stencil using an LM filled airbrush (Fig. 1c). This process can not only substantially reduce LM design printing time but can also help in recycling of deposited LM on the positive space of stencils [58]. As the target LM design is a grid structure, the corresponding ideal stencil would consist of numerous unconnected islands to generate the negative space through which the LM is supposed to be spray coated (Fig. S1). However, in practical case, attaining such stencil designs is impossible, as the positive components of such a stencil will have no physical connections with each other and the stencil frame. In order to address this problem, the stencil is designed in the form of parallel positive and negative spaces, and by spray coating the LM through the stencil by rotating at 90° to the initial deposited LM patterned on the substrate, intersecting LM grid patterns can be generated. This feat was possible due to the superior surface adhesion of LM on elastomer surface over the stencil (discussed later in this section). As the LM exits the airbrush upon release of compressed air, the air flow breaks the LM into small particles that stick on the substrate by virtue of the adhesive oxide layers realizing an LM film. Once the LM grid patterns were formed by removing the stencil, uncured silicone elastomer was spin-coated to encapsulate the LM grid patterns. The adhesion of oxide layer on elastomer prevents the LM design from shifting against the forces during the spin-coating process and the arising friction force from the encapsulating elastomer. The thicknesses of the encapsulating layers can be precisely

controlled by manipulating the spin-coating speed, as illustrated in Fig. S2. The film thickness (h) can be theoretically predicted using the Meyerhofer model, as represented by the modified equation [59]:

$$h = \frac{h_0}{\sqrt{1 + \frac{4\rho W^2 h_0^2 t}{3\mu}}} \qquad (8)$$

where the h_0 is the initial thickness of the coating material. The ultimate thickness of the film is predominantly influenced by the angular velocity and time, with these factors exerting a more substantial impact than other variables. Given that $W = \frac{\pi}{30} \times \varpi$, where the ϖ is the number of revolutions per minute. So, the ultimate thickness of the film can be conceptualized as a bivariate function dependent on both time (t) and angular velocity (ϖ) [59].

As described previously, a two-step spray coating process was adopted to form LM grid patterns (Fig. 2a) on various substrates. In order to ascertain the superior adhesion of LM on elastomer over stencil, a simple place-and-pick test was carried where an LM droplet was placed on one's surface and the other's surface was brought in contact and removed. As shown in Fig. 2b, c, the LM exhibited low surface adhesion to the OHP film stencil. On comparing the tilting angles initiating slide of LM on the silicone elastomer and OHP film, it was observed that the LM droplet remained on the silicone surface until the tilting angle reached 90° (Fig. 2d). However, the LM droplet began to slide when the tilting angle on the OHP film (Fig. 2e) reached 45°, indicating the inferior adhesion of the LM on the OHP surface. This ensured that when the OHP stencil is removed from the DragonSkin substrate after spray coating LM, the LM adhered exclusively to the substrate's surface, preserving the integrity of LM patterns. Therefore, the OHP stencil that was used to pattern the first set of parallel lines could be rotated at 90° to spray the second set of parallel lines perpendicular to the first set, resulting in LM grid patterns by a two-step spray coating on various substrates, including silicones (Ecoflex 00–30, Exsil 100, Sylgard-184), glass, paper, low-density polyethylene (LDPE), fabric, nitrile gloves, and wood (Fig. 2f). These grid patterns can also be formed using different methods, including vacuum-assisted filling [60], injection and molding using an elastomeric stamp [61], and direct printing [62]. However, the two-step spray coating of LMs directly forms multi-junctioned LM patterns on various substrates without using any complicated printing or lithographic methods. Spray coating using an airbrush atomizes
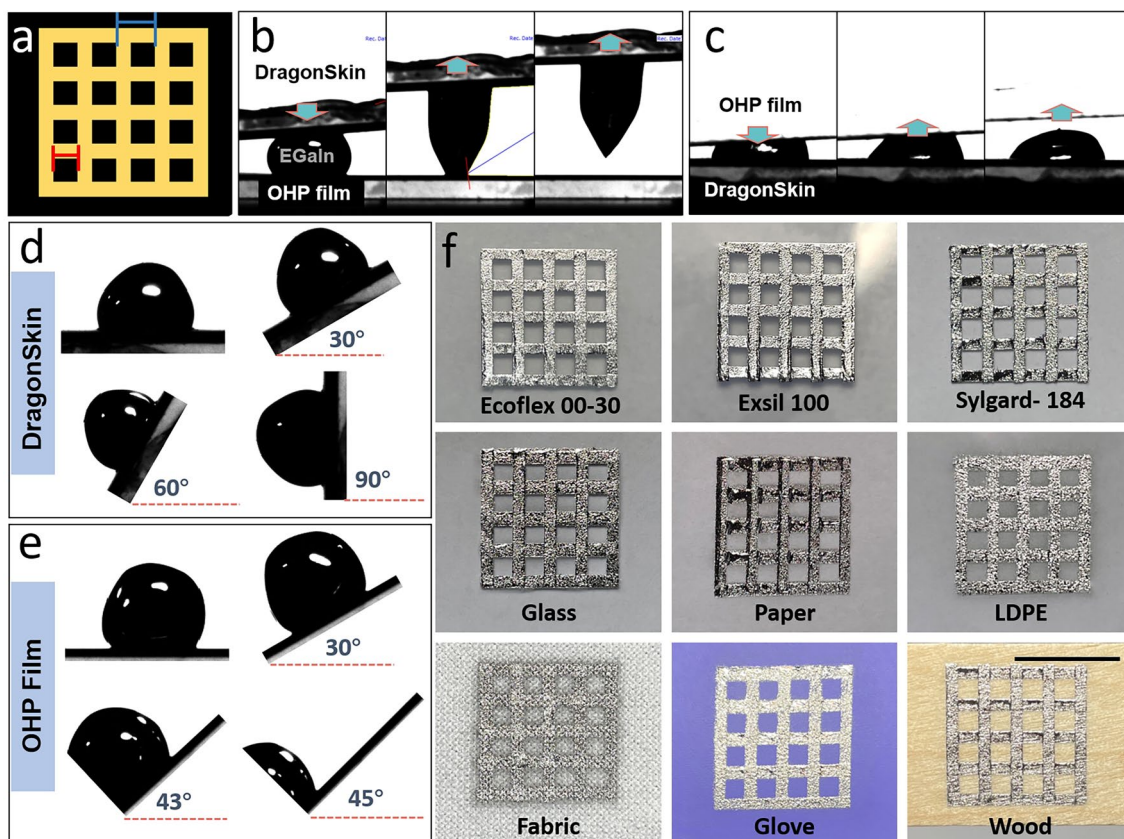
Fig. 2 **a** Illustration showing the design parameters of LM grid patterns. The blue and red scales represent grid spacing and grid gap respectively. **b**, **c** Adhesive properties of the LM on DragonSkin (silicone elastomer) and OHP film, respectively. **d**, **e** Tilting angles of LM to initiate sliding on **d** DragonSkin and **e** OHP surfaces. **f** LM grid patterns formed by two-step spray coating on various substrates, including silicones elastomers (Ecoflex 00–30, Exsil 100 and Sylgard-184), glass, paper, low-density polyethylene (LDPE), fabric, nitrile glove, and wood. The scale bar is 1 cm

the LM into small droplets with a thin oxide layer (1–3 nm) on the surface, resulting in a higher surface-to-volume ratio of the oxide layer, compared with the rheologically oxidized LM paste patterned on the surface using a brush [63]. This allowed consistent contact of the LM with the silicone substrate without displacement or aggregation, even after spin coating at a rate of up to 3,000 rpm and repeated stretching cycles (Fig. S3). In addition, the thickness of the LM layer can be precisely controlled by manipulating the airbrush–substrate distance and the spray coating duration (Fig. S4). Also, the stencils can be recycled by first removing the LM deposited on the stencil by simply swiping with an aqueous 0.1 M hydrochloric acid solution saturated cotton swab and finally washing the stencil surface with detergent (Fig. S5).

3.2 Mechanical Properties of LMGDs

In order to achieve multiple internal reflections of incident electromagnetic waves (EMW), a secondary LM layer was stencil printed on the described grid structure and encapsulated (discussed in the next section). To demonstrate high deformability of the LMGDs, ultrastretchable and soft silicone (DragonSkin) with high elongation at break (1000%) and a low modulus (0.5 MPa) was chosen [57]. DragonSkin exhibits remarkable flexibility allowing it to seamlessly conform to diverse surfaces when utilized as a mountable device. Additionally, the incorporation of LM within DragonSkin does not impede the device's ability to deform, ensuring optimal adaptability during use. Figure 3a–i shows the 410-µm-thick LMGD stretched uniaxially up to 400% by a manual stretcher, where the embedded liquid metal designs were observed to stretch accordingly while maintaining
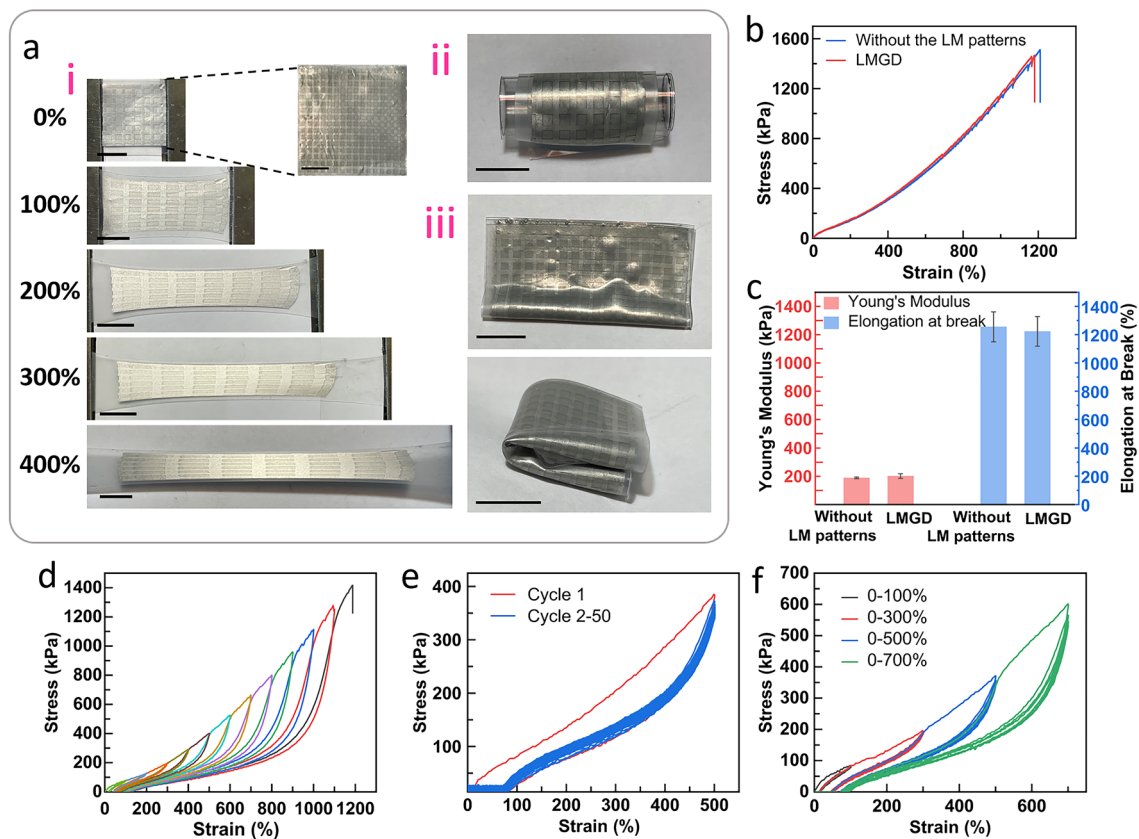
Fig. 3 **a** Photographs showing deformability of the LMGD: (i) stretchability (400%), (ii) rollability, and (iii) foldability. The scale bar is 2 cm. **b** Stress–strain curve of the LMGD and silicone elastomer film without the LM patterns. **c** Young's modulus and elongation at break of the LMGD and silicone elastomer film without the LM patterns. Stress–strain curves of **d** LMGD for progressive tensile strains with single cycle from 0 to 1200% at the intervals of 100%, **e** LMGD during consecutive 50 cycles of strains at 500%, and **f** LMGD for repeated progressive tensile strains with five cycles for strain values of 100%, 300%, 500%, and 700%

interconnected electrode networks upon strain. Similarly, Fig. 3a-ii,iii show the states of the device in rolled and folded states respectively. Next, the device was subjected to uniaxial stretching in order to compare its mechanical properties with its unpatterned elastomer counterpart. The presence of the LM patterns slightly increased Young's modulus (from 188.7 ± 5.9 to 201.4 ± 10 kPa) and decreased the elongation at break (from $1255 \pm 105\%$ to $1223 \pm 104\%$) (Fig. 3b, c) owing to the stiffening effect from increased oxide layer due to spray coating [64, 65], and fracturing along the pattern respectively. When the strain value of both LMGD and unpatterned film approached near 600%–800%, fine sawtooth patterns could be observed in the stress–strain curve. This phenomenon is presumably due the fact that since the samples have three layers of elastomers, there are two elastomeric interfaces which might have suffered slight microscopic interfacial delamination at very high strain values.

Next, the LMGD was subjected to a series of cyclic loading and unloading tests in order to ascertain its durability and longtime usability. First, as shown in Fig. 3d, the LMGD was subjected to progressing cyclic test involving a step-wise increment 100% strain till break at about 1200%. A few distinct sawtooth patterns were observed at higher strain values suggesting microscopic interfacial delamination. This was followed by 50 cycles of loading–unloading upto 500% and subsequent step-wise cyclic tests involving five cycles each till 700% of another identical LMGD sample (Fig. 3e, f). As seen in the graphs, the LMGD was elastically reversible due to minimal changes in the silicone polymeric network and rheological properties of the LM during strains. After the cycling tests, the LMGD exhibited a slight longitudinal deformation close to 5% (Fig. S6) occurring during the initial loading of the strain on the sample leading to some irreversible plastic deformation that can be attributed to the Mullins effect.

3.3 EMI Shielding Performance of LMGDs

Considering the fact that due to the extreme deformability of both LM and elastomer, LM-patterned devices can exhibit good metallic conductivity even under strain [66–68], the LMGD was utilized as a soft and stretchable EMI shielding material. As illustrated in Fig. 1b, the device consisted of three elastomer layers, out of which the top and bottom elastomer layers are meant for device encapsulation while the middle elastomer acts as the physical barrier between the LM layer and the LM grid pattern. This multilayered structure can effectively shield against EMI through multiple reflections of the EMWs within the device. In order to understand the shielding properties of the individual LM layers, the (SE) of both layers was tested. The LM thin layer exhibited a high EMI (SE_T) more than 20 dB (Fig. 4a), whereas the LM grid patterns resulted in near-zero (SE_R) at the resonant frequency (Fig. 4b). The phenomenon is pictorially depicted in Fig. S7. Thus, by combining these layers, the EMWs are transmitted through the elastomer between the LM grid patterns but are reflected and absorbed by the thin LM layer in the polymer matrix by the multiple reflection and absorption between the two LM layers. The LMGD with a grid spacing of 3 mm showed a high shielding capability (SE_T of 75 dB) at frequencies ranging from 50 to 110 GHz (Fig. 4c), owing to the multiple reflections and absorption of the EMWs between the layers. In particular, the minimum SE_R was only 1.4 dB at a frequency of 81.3 GHz (Fig. 4d), which corresponds well with the results of theoretical calculations (Note S1 and Table S1).

In addition, the grid spacings of LMGD can be manipulated upon stretching the device in the direction parallel to the electrodes. Using the LMGD with an initial grid spacing of 3 mm, when a strain value of 33% was applied to the device, shifting in the resonant frequency occurred from 81.3 to 71.3 GHz (Fig. 4e). Theoretically, at this strain value, the grid spacing should increase to 4 mm; however, under practical cases, the width of the lines of LM grid would also
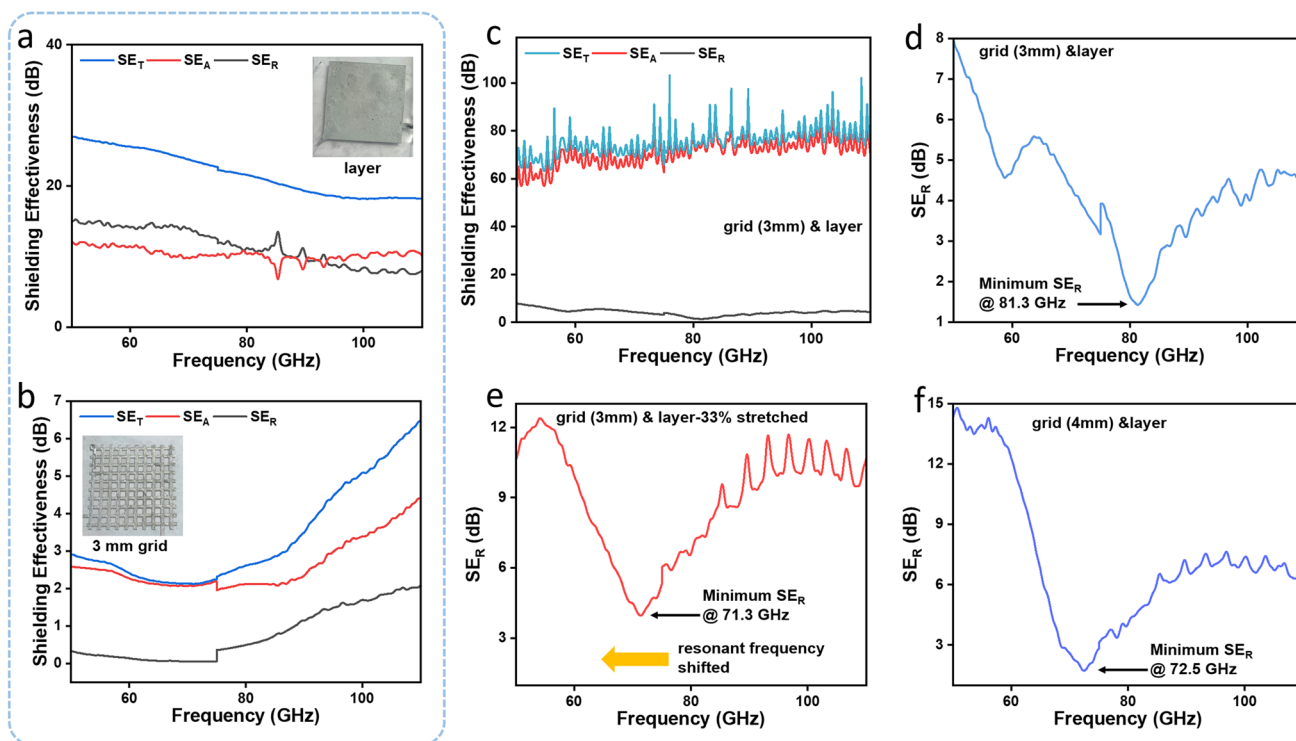

Fig. 4 **a** EMI (SE) of LM layer for EMWs at 50–110 GHz. **b** EMI (SE) of LM grid pattern with a grid spacing of 3 mm for EMWs at 50–110 GHz. **c** EMI (SE) and **d** reflection (SE_R) of the 410-μm-thick LMGD with a grid spacing of 3 mm for EMWs at 50–110 GHz. **e** SE_R of the 410-μm-thick LMGD with a grid spacing of 3 mm when subjected to a strain of 33% for EMWs at 50–110 GHz. **f** SE_R of the 410-μm-thick LMGD with a grid spacing of 4 mm for EMWs at 50–110 GHz
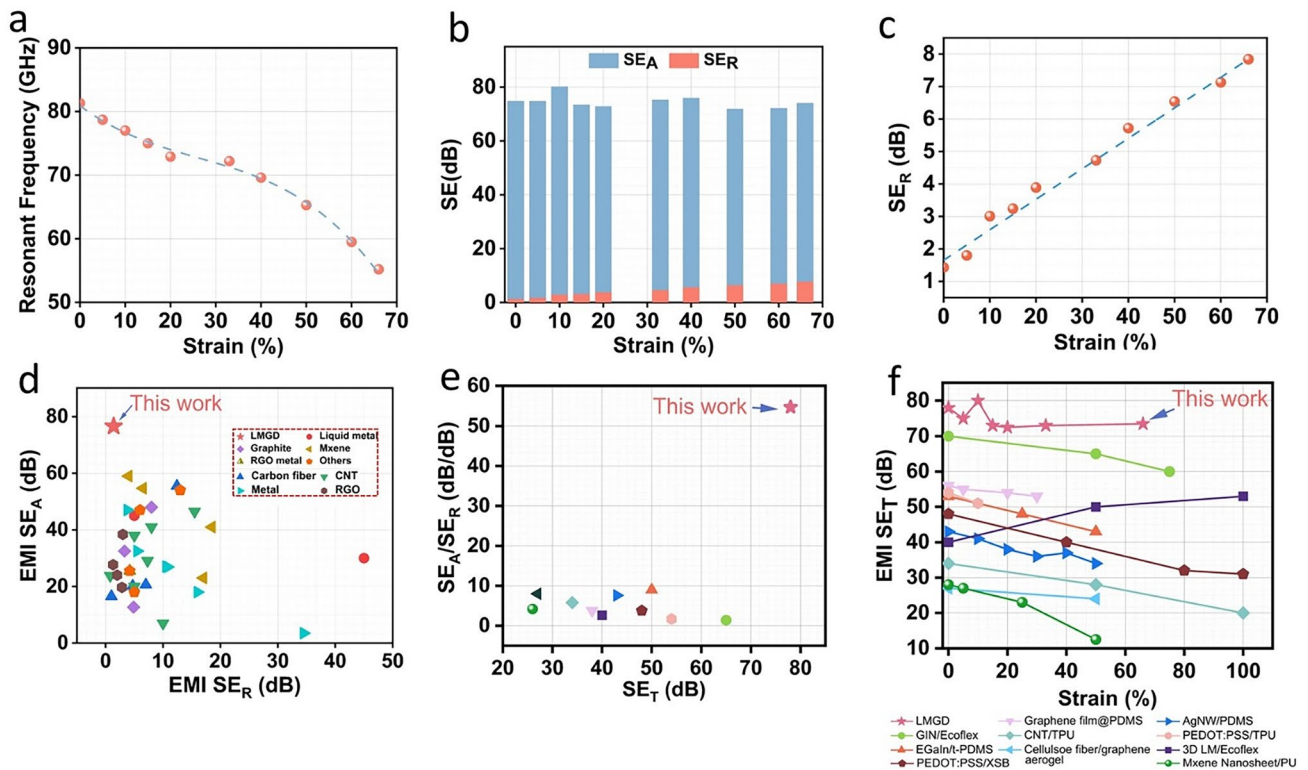
Fig. 5 **a** Comparative analysis of resonant frequencies of the LMGD subjected to tensile strain from 0 to 66%. **b** EMI SE, including SE_R and SE_A of the LMGD, averaged over frequencies 50–110 GHz at strains of 0–66%. **c** EMI SE_R of the LMGD with a grid spacing of 3 mm under the loading tensile strain of up to 66%. **d** Comparison of SE_A of various EMI shielding materials, including metals (Ni-Co, Ag, and Cu nanowires) and others (carbon aerogel, $Fe_2H_2NiO_4$, and Fe_2O_3), as a function of SE_R. **e** Comparison of the SE_A/SE_R of various stretchable EMI shieling materials as a function of SE_T. **f** Comparison of the SE_T of various stretchable EMI shieling materials as a function of strain. The results were collected from previous studies, as shown in Tables S2–S4

stretch by an identical strain value. To verify the consistency of the resonant frequency shifting, SE_R of another LMGD with an initial grid spacing of 4 mm was measured whose resonant frequency was found to be 72.5 GHz (Fig. 4f) which is only 1.68% higher than the value obtained when the LMGD with 3-mm grid spacing was stretched to 33%. This ability to tune the resonant frequency upon stretching enables the LMGD to be utilized as a stretchable electromagnetic shielding material that can effectively function as a frequency pass filter for EMWs [55, 69].

To investigate the effects of mechanical stretching of the device on EMI shielding effectiveness (SE) and corresponding resonant frequencies, the LMGD was subjected to a strain of up to 66%, and the corresponding EMI shielding properties were measured. As illustrated in Fig. 5a, the resonant frequency decreased monotonically with increasing strain, whereas SE_T remained at a high average of 75 dB (Fig. 5b) which is well match with the theoretical results

(Table S1). There was a slight increase in the SE_R and a corresponding decrease in the SE_A while the strain increased, presumably owing to the decreased cross-sectional area of the polymer matrix during stretching. Upon strain, the EMW reflected from the LM layers directly propagated backward to the EMW source, resulting in a lower SE_A and a higher SE_R for the LMGD (Fig. 5c). Interestingly, at a strain value of 10%, the resonant frequency recorded 77 GHz, which corresponds to automotive radar band used in self-driving cars with ADAS [51, 52]. Thus, it can be inferred that the shielding properties of the LMGD can be tuned by mere stretching to meet a certain target resonant frequency.

To investigate the durability of the LMGD, changes in the SE and effective resistance upon repeated loading and unloading tensile strain of 100% over 100 cycles were monitored (Fig. S8). The average (SE_T) after 100 cycles of strain was approximately 70 dB, which is similar to that of LMGD prior to the application of the tensile strain (Fig. S8a, b),

owing to preserved geometries of the electrodes even after cycles of strain. However, repeated loading and unloading strains could cause the oxide layer to break and reform; thus, it may accumulate on the LM surface, resulting in a thicker oxide layer and increased effective resistance (Fig. S8c, d).

Figure 5d compares the SE_A and SE_R values of LMGD with previously reported studies. To the best of our knowledge, the LMGD developed in this work exhibits the best SE in terms of low reflection and high absorption properties reported to date. A detailed comparison of the various materials used along with thickness of the fabricated devices as well as the shielding properties is given in Table S2. Although previous studies on EMI shielding have mostly focused on improving the SE_A without considering the reduction in the SE_R, high reflection can act as a source of EM pollution that interferes with other components. As shown in Fig. 5e, LMGD exhibited the highest SE_A to SE_R ratio (54.7) and SE_T (78 dB) when compared to previous studies on stretchable EMI shielding materials. A detailed comparison of the shielding properties of these stretchable devices with LMGD is provided in Table S3. Additionally, Fig. 5f compares the SE_T of LMGD with those of previously reported stretchable EMI shielding materials when subjected to strain. While most materials exhibit a decrease in SE_T upon straining, LMGDs can maintain high SE_T stability even under large external deformations. The corresponding table of comparison of SE_T of these materials along with their reported strain values is given in Table S4. As a practical demonstration (Fig. S9), the LMGD can also effectively shield the EMWs emitted from the Tesla coil, thereby preventing the flow of induced currents and deactivating the light. However, the applicability of such grid structures is not only limited to EMI shielding but can also be extended to other applications, e.g., biomechanical sensing (Fig. S10).

4 Conclusions

In this work, soft and stretchable electromagnetic interference shielding thin film device (LMGD) is developed by leveraging stretchable and soft behaviors of both liquid metal and silicone elastomer. The LMGD could achieve high EMI shielding effectiveness (SE_T up to 75 dB) with high absorption and low reflectance (SE_R of 1.5 dB at the resonant frequency) owing to multiple internal reflections in the frequency range of 50–110 GHz by virtue of strategically patterned LM grid design. By taking advantage of higher surface adhesion of LM on elastomer, the grid design could be obtained by a dual-step aerosol deposition process through recyclable stencils, which is both rapid and cost-effective compared to prevalent printing techniques. The stretchable and elastic properties of the device facilitated strain-induced adjustment of grid spacings, resulting in a shift in the resonant frequency, thereby making it possible to achieve strain-tunable EMI shielding abilities. On stretching the LMGD to 10%, the resonant frequency shifted to 77 GHz, which corresponds to automotive radar band used in self-driving cars with ADAS. The LMGD could also retain its shielding properties even after multiple strain cycles, proving its durability and longtime usability. This thin film-shaped LMGD along with its ability to tune EMI shielding properties would be utilized as a powerful EMI shielding material for the next-generation electronic devices.

Declarations

References

1. C. Mo, X. Lei, X. Tang, M. Wang, E.-T. Kang et al., Nanoengineering natural leather for dynamic thermal management and electromagnetic interference shielding. Small **19**, e2303368 (2023). https://doi.org/10.1002/smll.202303368

2. H. Liu, Y. Xu, K. Yang, H. Hong, Y. Huang et al., Skin-like copper/carbon nanotubes/graphene composites and low thermogenesis during electromagnetic interference shielding. J. Mater. Chem. C **11**, 3010–3019 (2023). https://doi.org/10.1039/D2TC04552D

3. B. Yang, H. Wang, M. Zhang, F. Jia, Y. Liu et al., Mechanically strong, flexible, and flame-retardant $Ti_3C_2T_x$ MXene-coated aramid paper with superior electromagnetic interference shielding and electrical heating performance. Chem. Eng. J. **476**, 146834 (2023). https://doi.org/10.1016/j.cej.2023.146834

4. Y. Zhan, C. Santillo, Y. Meng, M. Lavorgna, Recent advances and perspectives on silver-based polymer composites for electromagnetic interference shielding. J. Mater. Chem. C **11**, 859–892 (2023). https://doi.org/10.1039/d2tc03821h

5. S. Zheng, Y. Wang, Y. Zhu, C. Zheng, Recent advances in structural design of conductive polymer composites for electromagnetic interference shielding. Polym. Compos. **45**, 43–76 (2024). https://doi.org/10.1002/pc.27773

6. A.A. Albert, V. Parthasarathy, P.S. Kumar, Review on recent progress in epoxy-based composite materials for Electromagnetic Interference (EMI) shielding applications. Polym. Compos. **45**, 1956–1984 (2024). https://doi.org/10.1002/pc.27928

7. X. Zhang, K. Qian, J. Fang, S. Thaiboonrod, M. Miao et al., Synchronous deprotonation–protonation for mechanically robust chitin/aramid nanofibers conductive aerogel with excellent pressure sensing, thermal management, and electromagnetic interference shielding. Nano Res. **17**, 2038–2049 (2024). https://doi.org/10.1007/s12274-023-6189-6

8. J. Xiao, B. Zhan, M. He, X. Qi, X. Gong et al., Interfacial polarization loss improvement induced by the hollow engineering of necklace-like PAN/carbon nanofibers for boosted microwave absorption. Adv. Funct. Mater. (2024). https://doi.org/10.1002/adfm.202316722

9. C. Li, L. Zhang, S. Zhang, Q. Yu, D. Li et al., Flexible regulation engineering of titanium nitride nanofibrous membranes for efficient electromagnetic microwave absorption in wide temperature spectrum. Nano Res. **17**, 1666–1675 (2024). https://doi.org/10.1007/s12274-023-6350-2

10. T. Zhao, J. Zhou, W. Wu, K. Qian, Y. Zhu et al., Antibacterial conductive polyacrylamide/quaternary ammonium chitosan hydrogel for electromagnetic interference shielding and strain sensing. Int. J. Biol. Macromol. **265**, 130795 (2024). https://doi.org/10.1016/j.ijbiomac.2024.130795

11. Y. Yao, S. Jin, H. Zou, L. Li, X. Ma et al., Polymer-based lightweight materials for electromagnetic interference shielding: a review. J. Mater. Sci. **56**, 6549–6580 (2021). https://doi.org/10.1007/s10853-020-05635-x

12. Y. Zhang, Z. Yang, Y. Yu, B. Wen, Y. Liu et al., Tunable electromagnetic interference shielding ability in a one-dimensional bagasse fiber/polyaniline heterostructure. ACS Appl. Polym. Mater. **1**, 737–745 (2019). https://doi.org/10.1021/acsapm.8b00025

13. X. Hou, X.-R. Feng, K. Jiang, Y.-C. Zheng, J.-T. Liu et al., Recent progress in smart electromagnetic interference shielding materials. J. Mater. Sci. Technol. **186**, 256–271 (2024). https://doi.org/10.1016/j.jmst.2024.01.008

14. X. Liu, Y. Li, X. Sun, W. Tang, G. Deng et al., Off/on switchable smart electromagnetic interference shielding aerogel. Matter **4**, 1735–1747 (2021). https://doi.org/10.1016/j.matt.2021.02.022

15. H. Wang, X. Ren, F. Wu, S. Zhang, L. Fang, Investigation on high EMI shielding effectiveness and shielding mechanism of spherical $Ti_3C_2T_x$ microfilm prepared by spray-freezing. J. Alloys Compd. **976**, 173317 (2024). https://doi.org/10.1016/j.jallcom.2023.173317

16. L. Liu, X. Chen, J. Wang, L. Qiao, S. Gao et al., Effects of Y and Zn additions on electrical conductivity and electromagnetic shielding effectiveness of Mg-Y-Zn alloys. J. Mater. Sci. Technol. **35**, 1074–1080 (2019). https://doi.org/10.1016/j.jmst.2018.12.010

17. U. Hwang, J. Kim, M. Seol, B. Lee, I.-K. Park et al., Quantitative interpretation of electromagnetic interference shielding efficiency: is it really a wave absorber or a reflector? ACS Omega **7**, 4135–4139 (2022). https://doi.org/10.1021/acsomega.1c05657

18. J. Lee, Y. Liu, Y. Liu, S.-J. Park, M. Park et al., Ultrahigh electromagnetic interference shielding performance of lightweight, flexible, and highly conductive copper-clad carbon fiber nonwoven fabrics. J. Mater. Chem. C **5**, 7853–7861 (2017). https://doi.org/10.1039/C7TC02074K

19. K. Chizari, M. Arjmand, Z. Liu, U. Sundararaj, D. Therriault, Three-dimensional printing of highly conductive polymer nanocomposites for EMI shielding applications. Mater. Today Commun. (2017). https://doi.org/10.1016/j.mtcomm.2017.02.006

20. B. Shen, Y. Li, W. Zhai, W. Zheng, Compressible graphene-coated polymer foams with ultralow density for adjustable electromagnetic interference (EMI) shielding. ACS Appl. Mater. Interfaces **8**, 8050–8057 (2016). https://doi.org/10.1021/acsami.5b11715

21. Y. Chen, H.-B. Zhang, Y. Yang, M. Wang, A. Cao et al., High-performance epoxy nanocomposites reinforced with three-dimensional carbon nanotube sponge for electromagnetic interference shielding. Adv. Funct. Mater. **26**, 447–455 (2016). https://doi.org/10.1002/adfm.201503782

22. F. Peng, W. Zhu, Y. Fang, B. Fu, H. Chen et al., Ultralight and highly conductive silver nanowire aerogels for high-performance electromagnetic interference shielding. ACS Appl. Mater. Interfaces **15**, 4284–4293 (2023). https://doi.org/10.1021/acsami.2c16940

23. Z. Lei, W. Liu, W. Xing, Y. Zhang, Y. Liu et al., Developing thermal regulating and electromagnetic shielding nacre-inspired graphene-conjugated conducting polymer film via apparent wiedemann-franz law. ACS Appl. Mater. Interfaces **14**, 49199–49211 (2022). https://doi.org/10.1021/acsami.2c14805

24. H. Lee, S.H. Ryu, S.J. Kwon, J.R. Choi, S.-B. Lee et al., Absorption-dominant mmWave emi shielding films with ultralow reflection using ferromagnetic resonance frequency tunable M-type ferrites. Nano-Micro Lett. **15**, 76 (2023). https://doi.org/10.1007/s40820-023-01058-w

25. J. Zhao, Z. Gu, Q., Zhang stacking MoS_2 flower-like microspheres on pomelo peels-derived porous carbon nanosheets for high-efficient X-band electromagnetic wave absorption. Nano Res. **17**, 1607–1615 (2024). https://doi.org/10.1007/s12274-023-6090-3

26. J. Zhao, M. Li, X. Gao, Construction of SnO_2 nanoparticle cluster@PANI core-shell microspheres for efficient X-band electromagnetic wave absorption. J. Alloys Compd. **915**, 165439 (2022). https://doi.org/10.1016/j.jallcom.2022.165439

27. X. Zhong, M. He, C. Zhang, Y. Guo, J. Hu et al., Heterostructured BN@Co-C@C endowing polyester composites excellent thermal conductivity and microwave absorption at C band. Adv. Funct. Mater. **34**, 2313544 (2024). https://doi.org/10.1002/adfm.202313544

28. M. He, J. Hu, H. Yan, X. Zhong, Y. Zhang et al., Shape anisotropic chain-like CoNi/polydimethylsiloxane composite films with excellent low-frequency microwave absorption and high thermal conductivity. Adv. Funct. Mater. (2024). https://doi.org/10.1002/adfm.202316691

29. S.H. Ryu, B. Park, Y.K. Han, S.J. Kwon, T. Kim et al., Electromagnetic wave shielding flexible films with near-zero reflection in the 5G frequency band. J. Mater. Chem. A **10**, 4446–4455 (2022). https://doi.org/10.1039/D1TA10065C

30. A. Sheng, W. Ren, Y. Yang, D.-X. Yan, H. Duan et al., Multilayer WPU conductive composites with controllable electro-magnetic gradient for absorption-dominated electromagnetic interference shielding. Compos. Part A Appl. Sci. Manuf. **129**, 105692 (2020). https://doi.org/10.1016/j.compositesa.2019.105692

31. W.-L. Song, M.-S. Cao, M.-M. Lu, S. Bi, C.-Y. Wang et al., Flexible graphene/polymer composite films in sandwich structures for effective electromagnetic interference shielding. Carbon **66**, 67–76 (2014). https://doi.org/10.1016/j.carbon.2013.08.043

32. Z. Wang, X. Zhang, C. Cheng, X. Song, C. Hua et al., 3D printed epoxy composite microsandwich with high strength, toughness, and EMI shielding performances. Compos. Struct. **323**, 117456 (2023). https://doi.org/10.1016/j.compstruct.2023.117456

33. X. Li, X. Ma, H. Zhang, N. Xue, Q. Yao et al., Ambient-stable MXene with superior performance suitable for widespread applications. Chem. Eng. J. **455**, 140635 (2023). https://doi.org/10.1016/j.cej.2022.140635

34. T. Habib, X. Zhao, S.A. Shah, Y. Chen, W. Sun et al., Oxidation stability of Ti_3C_2Tx MXene nanosheets in solvents and composite films. npj 2D Mater. Appl. **3**(1): 8 (2019). https://doi.org/10.1038/s41699-019-0089-3

35. R. Tutika, A.B.M.T. Haque, M.D. Bartlett, Self-healing liquid metal composite for reconfigurable and recyclable soft electronics. Commun. Mater. **2**, 64 (2021). https://doi.org/10.1038/s43246-021-00169-4

36. M.D. Bartlett, A. Fassler, N. Kazem, E.J. Markvicka, P. Mandal et al., Stretchable, high-*k* dielectric elastomers through liquid-metal inclusions. Adv. Mater. **28**, 3726–3731 (2016). https://doi.org/10.1002/adma.201506243

37. A.B.M. Tahidul Haque, D. Ho, D. Hwang, R. Tutika, C. Lee et al., Electrically conductive liquid metal composite adhesives for reversible bonding of soft electronics. Adv. Funct. Mater. (2023). https://doi.org/10.1002/adfm.202304101

38. W. Zhang, J.Z. Ou, S.-Y. Tang, V. Sivan, D.D. Yao et al., Liquid metal/metal oxide frameworks. Adv. Funct. Mater. **24**, 3799–3807 (2014). https://doi.org/10.1002/adfm.201304064

39. V. Sivan, S.-Y. Tang, A.P. O'Mullane, P. Petersen, N. Eshtiaghi et al., Liquid metal marbles. Adv. Funct. Mater. **23**, 144–152 (2013). https://doi.org/10.1002/adfm.201200837

40. T. Daeneke, K. Khoshmanesh, N. Mahmood, I.A. de Castro, D. Esrafilzadeh et al., Liquid metals: fundamentals and applications in chemistry. Chem. Soc. Rev. **47**, 4073–4111 (2018). https://doi.org/10.1039/c7cs00043j

41. G. Li, M. Zhang, S. Liu, M. Yuan, J. Wu et al., Three-dimensional flexible electronics using solidified liquid metal with regulated plasticity. Nat. Electron. **6**, 154–163 (2023). https://doi.org/10.1038/s41928-022-00914-8

42. T. Wang, S. Liu, Y. Hu, Z. Xu, S. Hu et al., Liquid metal/wood anisotropic conductors for flexible and recyclable electronics. Adv. Mater. Interfaces **9**, 2200172 (2022). https://doi.org/10.1002/admi.202200172

43. Q. Shen, M. Jiang, R. Wang, K. Song, M.H. Vong et al., Liquid metal-based soft, hermetic, and wireless-communicable seals for stretchable systems. Science **379**, 488–493 (2023). https://doi.org/10.1126/science.ade7341

44. B. Yao, W. Hong, T. Chen, Z. Han, X. Xu et al., Highly stretchable polymer composite with strain-enhanced electromagnetic interference shielding effectiveness. Adv. Mater. **32**, e1907499 (2020). https://doi.org/10.1002/adma.201907499

45. M. Zhang, P. Zhang, Q. Wang, L. Li, S. Dong et al., Stretchable liquid metal electromagnetic interference shielding coating materials with superior effectiveness. J. Mater. Chem. C **7**, 10331–10337 (2019). https://doi.org/10.1039/C9TC02887K

46. L.-C. Jia, X.-X. Jia, W.-J. Sun, Y.-P. Zhang, L. Xu et al., Stretchable liquid metal-based conductive textile for electromagnetic interference shielding. ACS Appl. Mater. Interfaces **12**, 53230–53238 (2020). https://doi.org/10.1021/acsami.0c14397

47. W. Xing, Y. Xu, S. Chen, Z. Lei, Y. Zhang et al., Cuttlefish-inspired self-adaptive liquid metal network enabling electromagnetic interference shielding and thermal management. Adv. Mater. Technol. **8**, 2300102 (2023). https://doi.org/10.1002/admt.202300102

48. X. Sun, J.-H. Fu, C. Teng, M. Zhang, T. Liu et al., Superhydrophobic E-textile with an Ag-EGaIn conductive layer for motion detection and electromagnetic interference shielding. ACS Appl. Mater. Interfaces **14**, 33650–33661 (2022). https://doi.org/10.1021/acsami.2c09554

49. O. Pitkänen, J. Tolvanen, I. Szenti, Á. Kukovecz, J. Hannu et al., Lightweight hierarchical carbon nanocomposites with highly efficient and tunable electromagnetic interference

shielding properties. ACS Appl. Mater. Interfaces **11**, 19331–19338 (2019). https://doi.org/10.1021/acsami.9b02309

50. B. Zhao, R. Wang, Y. Li, Y. Ren, X. Li et al., Dependence of electromagnetic interference shielding ability of conductive polymer composite foams with hydrophobic properties on cellular structure. J. Mater. Chem. C **8**, 7401–7410 (2020). https://doi.org/10.1039/D0TC00987C

51. M.C. Vu, P.J. Park, S.-R. Bae, S.Y. Kim, Y.-M. Kang et al., Scalable ultrarobust thermoconductive nonflammable bioinspired papers of graphene nanoplatelet crosslinked aramid nanofibers for thermal management and electromagnetic shielding. J. Mater. Chem. A **9**, 8527–8540 (2021). https://doi.org/10.1039/D0TA12306D

52. J. Hasch, E. Topak, R. Schnabel, T. Zwick, R. Weigel et al., Millimeter-wave technology for automotive radar sensors in the 77 GHz frequency band. IEEE Trans. Microw. Theory Tech. **60**, 845–860 (2012). https://doi.org/10.1109/TMTT.2011.2178427

53. A.M. Nicolson, G.F. Ross, Measurement of the intrinsic properties of materials by time-domain techniques. IEEE Trans. Instrum. Meas. **19**, 377–382 (1970). https://doi.org/10.1109/TIM.1970.4313932

54. H. Abbasi, M. Antunes, J.I. Velasco, Recent advances in carbon-based polymer nanocomposites for electromagnetic interference shielding. Prog. Mater. Sci. **103**, 319–373 (2019). https://doi.org/10.1016/j.pmatsci.2019.02.003

55. R. Ulrich, Far-infrared properties of metallic mesh and its complementary structure. Infrared Phys. **7**, 37–55 (1967). https://doi.org/10.1016/0020-0891(67)90028-0

56. P. Bhuyan, Y. Wei, D. Sin, J. Yu, C. Nah et al., Soft and stretchable liquid metal composites with shape memory and healable conductivity. ACS Appl. Mater. Interfaces **13**, 28916–28924 (2021). https://doi.org/10.1021/acsami.1c06786

57. S. Park, K. Mondal, R.M. Treadway, V. Kumar, S. Ma et al., Silicones for stretchable and durable soft devices: beyond sylgard-184. ACS Appl. Mater. Interfaces **10**, 11261–11268 (2018). https://doi.org/10.1021/acsami.7b18394

58. T.V. Neumann, B. Kara, Y. Sargolzaeiaval, S. Im, J. Ma et al., Aerosol spray deposition of liquid metal and elastomer coatings for rapid processing of stretchable electronics. Micromachines **12**, 146 (2021). https://doi.org/10.3390/mi12020146

59. U.G. Lee, W.-B. Kim, D.H. Han, H.S. Chung, A modified equation for thickness of the film fabricated by spin coating.

Symmetry **11**, 1183 (2019). https://doi.org/10.3390/sym11091183

60. Y. Lin, O. Gordon, M.R. Khan, N. Vasquez, J. Genzer et al., Vacuum filling of complex microchannels with liquid metal. Lab Chip **17**, 3043–3050 (2017). https://doi.org/10.1039/C7LC00426E

61. Y. Zhang, H. Duan, G. Li, M. Peng, X. Ma et al., Construction of liquid metal-based soft microfluidic sensors via soft lithography. J. Nanobiotechnology **20**, 246 (2022). https://doi.org/10.1186/s12951-022-01471-0

62. L. Wang, J. Liu, Pressured liquid metal screen printing for rapid manufacture of high resolution electronic patterns. RSC Adv. **5**, 57686–57691 (2015). https://doi.org/10.1039/C5RA10295B

63. C. Votzke, N. Alteir, Y. Mengüç, M.L. (2021). Johnston, Stenciled liquid metal paste for robust stretchable electrical interconnects. 2021 IEEE International Conference on Flexible and Printable Sensors and Systems (FLEPS). Manchester, United Kingdom. IEEE, pp.1–4

64. Y. Wei, S. Kim, S. Kim, P. Bhuyan, K. Hong et al., Liquid metal fillers enabled remote actuating and localizing reversible wrinkles on polymeric bilayer. Appl. Mater. Today **28**, 101537 (2022). https://doi.org/10.1016/j.apmt.2022.101537

65. R.W. Style, R. Boltyanskiy, B. Allen, K.E. Jensen, H.P. Foote et al., Stiffening solids with liquid inclusions. Nat. Phys. **11**, 82–87 (2015). https://doi.org/10.1038/nphys3181

66. H. Wang, R. Li, Y. Cao, S. Chen, B. Yuan et al., Liquid metal fibers. Adv. Fiber. Mater. **4**, 987–1004 (2022). https://doi.org/10.1007/s42765-022-00173-4

67. D. Sin, V.K. Singh, P. Bhuyan, Y. Wei, H.-M. Lee et al., Ultrastretchable thermo- and mechanochromic fiber with healable metallic conductivity. Adv. Electron. Mater. **7**, 2100146 (2021). https://doi.org/10.1002/aelm.202100146

68. M.D. Dickey, Stretchable and soft electronics using liquid metals. Adv. Mater. **29**, 1606425 (2017). https://doi.org/10.1002/adma.201606425

69. P.A.R. Ade, G. Pisano, C. Tucker, S. Weaver, A review of metal mesh filters. In: Zmuidzinas J, Holland WS, Withington S, Duncan WD (eds) *Millimeter and Submillimeter Detectors and Instrumentation for Astronomy* III. SPIE.